Journal of Controlled Release 359 (2023) 373–383

Contents lists available at ScienceDirect

Journal of Controlled Release

journal homepage: www.elsevier.com/locate/jconrel

Control of drug release kinetics from hot-melt extruded drug-loaded polycaprolactone matrices

Yun-Chu Chen [a], Sota Shishikura [a], Dana E. Moseson [a], Austin J. Ignatovich [a], Joshua Lomeo [b], Aiden Zhu [b], Sarena D. Horava [c], Coralie A. Richard [d], Kinam Park [a,e], Yoon Yeo [a,e,*]

[a] Department of Industrial and Physical Pharmacy, Purdue University, 575 Stadium Mall Drive, West Lafayette, IN 47907, USA
[b] DigiM Solution LLC, 500 West Cummings Park, Woburn, MA 01801, USA
[c] Eli Lilly and Company, 450 Kendall Street, Cambridge, MA 02142, USA
[d] Eli Lilly and Company, 893 Delaware Street, Indianapolis, IN 46225, USA
[e] Weldon School of Biomedical Engineering, Purdue University, West Lafayette, IN 47907, USA

ARTICLE INFO

Keywords:
Meloxicam
Hot-melt extrusion
Release kinetics control
Porogen
Artificial intelligence image analysis
Microstructure

ABSTRACT

Sustained local delivery of meloxicam by polymeric structures is desirable for preventing subacute inflammation and biofilm formation following tissue incision or injury. Our previous study demonstrated that meloxicam release from hot-melt extruded (HME) poly(ε-caprolactone) (PCL) matrices could be controlled by adjusting the drug content. Increasing drug content accelerated the drug release as the initial drug release generated a pore network to facilitate subsequent drug dissolution and diffusion. In this study, high-resolution micro-computed tomography (HR μCT) and artificial intelligence (AI) image analysis were used to visualize the microstructure of matrices and simulate the drug release process. The image analysis indicated that meloxicam release from the PCL matrix was primarily driven by diffusion but limited by the amount of infiltrating fluid when drug content was low (*i.e.*, the connectivity of the drug/pore network was poor). Since the drug content is not easy to change when a product has a fixed dose and dimension/geometry, we sought an alternative approach to control the meloxicam release from the PCL matrices. Here, magnesium hydroxide ($Mg(OH)_2$) was employed as a solid porogen in the drug-PCL matrix so that $Mg(OH)_2$ dissolved with time in the aqueous environment creating additional pore networks to facilitate local dissolution and diffusion of meloxicam. PCL matrices were produced with a fixed 30 wt% meloxicam loading and variable $Mg(OH)_2$ loadings from 20 wt% to 50 wt%. The meloxicam release increased in proportion to the $Mg(OH)_2$ content, resulting in almost complete drug release in 14 d from the matrix with 50 wt% $Mg(OH)_2$. The porogen addition is a simple strategy to tune drug release kinetics, applicable to other drug-eluting matrices with similar constraints.

1. Introduction

Drug-eluting polymeric structures are widely used in medical applications where sustained local drug delivery is desired [1]. Potential applications include the management of inflammations subsequent to tissue incision or suture injury and wound dressings that release anti-inflammatory or anti-infectious drugs over a defined period [2,3]. With spatiotemporal control of the release, these agents can protect the tissue injury site from further inflammation or infection and promote tissue regeneration, thereby minimizing the risks of off-target side effects and drug resistance due to excessive systemic exposure to the drug.

A drug of interest in wound management is the non-steroidal anti-inflammatory drug (NSAID) meloxicam, a relatively selective cyclo-oxygenase (COX)-2 inhibitor, which reduces the synthesis of lipid inflammatory mediators [4,5]. Meloxicam is indicated for the treatment of rheumatoid arthritis [6], osteoarthritis [7], ankylosing spondylitis [8], joint pain [9], and post-surgical inflammation [10]. Meloxicam is also expected to prevent biofilm formation on implanted devices or post-surgical wound dressings [11] and provide opioid-sparing post-operative analgesia [12,13]. For these purposes, a two-week sustained meloxicam delivery is desirable because most subacute inflammations and biofilm formations are likely to occur during this period [14–17]; moreover, the extended use of an NSAID may interfere with wound healing [18].

* Corresponding author at: Department of Industrial and Physical Pharmacy, Purdue University, 575 Stadium Mall Drive, West Lafayette, IN 47907, USA.
E-mail address: yyeo@purdue.edu (Y. Yeo).

https://doi.org/10.1016/j.jconrel.2023.05.049
Received 15 February 2023; Received in revised form 19 May 2023; Accepted 31 May 2023

Sustained local delivery of meloxicam may be accomplished by its encapsulation in biocompatible polymers, which can be fabricated into implants, fibers, or particles. Commonly used polymers include poly (lactic-*co*-glycolide) (PLGA), polylactide (PLA), polyglycolide (PGA), and polycaprolactone (PCL). These polymers control the drug release by serving as a diffusion barrier, where the barrier function may change with time as they swell and/or degrade. Previously, it was demonstrated that PCL was most appropriate for the sustained delivery of meloxicam among these polymers [19]. In that study, meloxicam was mixed with PCL and extruded through a hot-melt extruder to form a cylindrical matrix with the drug embedded in the polymer as solid clusters. Since the PCL matrix did not degrade within the time scale of interest, the drug release rate was dependent on the dissolution of drug clusters by the infiltrating fluid, followed by the diffusion of dissolved drug molecules through the polymer matrix. The drug content in the matrix played a major role in controlling the drug release rate, as the dissolving drug clusters generated fluid channels to facilitate additional fluid influx as well as drug dissolution and transport. Therefore, a higher drug content, and thereby a better-connected channel network, resulted in a faster drug release. Accordingly, a PCL matrix loaded with 65 wt% meloxicam completed the drug release in two weeks [19], which is the target period for applications in post-surgical wound management [20].

However, when the dose and dimension/geometry of the dosage forms are constrained by the type of applications (such as surgical staples and wound dressing), it is not feasible to control the drug release rate by the drug loading content alone. In this case, an alternative approach is needed to control the drug release rate. Therefore, we sought to control the drug release rate, independent of the drug content, by employing a sustained porogen, which dissolves in the PCL matrices over time and generates evolving pores in the PCL matrices to facilitate drug release.

In this study, the meloxicam-loaded PCL matrices were produced by a hot melt extruder in the shape of a thin cylinder with a dimension relevant to medical applications, such as surgical staples, sutures, and injectable implants. First, the effect of cylinder diameter size on the *in vitro* drug release profiles was investigated. High-resolution micro-computed tomography (HR μCT) and artificial intelligence (AI) image analysis were used to simulate drug release kinetics and understand the drug release process. Different salts were screened as porogens to facilitate drug release control. The salt-containing meloxicam/PCL matrices were characterized by solid-state analysis and multiple imaging techniques to investigate the drug state and the role of salt in the drug release control. The results of this study demonstrate the feasibility of tuning the drug release by salt porogens and the utility of imaging analysis in understanding the drug release process.

2. Materials and methods

2.1. Materials

Meloxicam (lot 2690001Y03F, 100.6% potency) was received from Olon Derivados Quimicos (Alcantarilla, Spain). Poly(ε-caprolactone) (PCL; Purasorb PC 17), magnesium hydroxide ($Mg(OH)_2$), sodium bicarbonate ($NaHCO_3$), zinc oxide (ZnO), phosphate-buffered saline (PBS tablets), tetrahydrofuran (THF), and Trizma base were obtained from Sigma-Aldrich (MilliporeSigma, Burlington, MA, USA). Magnesium phosphate ($Mg_3(PO_4)_2{\cdot}xH_2O$, ACROS Organics Chemicals), Dimethyl sulfoxide (DMSO, Fisher Chemical), and Tween 80 (Quality Biological Inc) were purchased from Thermo Fisher Scientific (Pittsburgh, PA).

2.2. Preparation of meloxicam/PCL matrices

Meloxicam/PCL HME matrices were prepared by the HAAKE™ MiniCTW Micro-Conical Twin Screw Compounder (Thermo Fisher Scientific, USA), co-rotated with screws in a 2 mL volume barrel. Salts ($Mg(OH)_2$, $NaHCO_3$, $Mg_3(PO_4)_2{\cdot}xH_2O$, and ZnO) were added as an optional ingredient. The meloxicam and polymer mixtures, with or without the salts, were processed at 20 rpm and 120 °C with a residence time (circulation time with closed valve before extrusion) of 5 min. The total extrusion time ranged from 3 to 10 min according to the die orifice diameter and the flow property of each sample. The total mass was fixed at 3 g, and the composition was varied. Meloxicam was a powder with a volume moment mean diameter $D_{[3,4]}$ of 7.46 ± 0.33 μm and was used as received. Meloxicam, PCL, and salts were combined according to the proportions described in Table 1 and extruded through a 2 mm or 0.5 mm die without milling or pre-processing. The matrices were named by the mass fraction of meloxicam (M#/PCL, # indicates wt% of meloxicam in each matrix). When a salt was included, the name was extended by the cation and its mass fraction, with the exception of $Mg_3(PO_4)_2{\cdot}xH_2O$, which was signified as MgPO (Table 1). For example, M30/PCL(MgPO35) represents a PCL matrix containing 30 wt% meloxicam and 35 wt% $Mg_3(PO_4)_2{\cdot}xH_2O$ with the remainder (35 wt%) filled with PCL.

2.3. In vitro meloxicam release kinetics

The meloxicam-PCL matrices, with or without salts, were cut into discs 2 mm in diameter × 0.7 mm in thickness or cylinders 0.5 mm in diameter × 10 mm in length (Supporting Fig. 1) with total sample weights of 2.8–3 mg. For dissolution testing, the samples were put in a 50 mL Falcon tube containing 40 or 50 mL of PBST, phosphate buffered (10 mM phosphate, pH 7.4) saline containing 0.1% Tween 80, and placed on an orbital shaker operating at 15 rpm and 37 °C. The ratio of meloxicam-to-release medium satisfied the sink condition (≤ 1/3 of saturation solubility [23]; saturation solubility of meloxicam in PBST at 37 °C: 0.099 ± 0.003 mg/mL [19]). A 0.5 mL volume of the release medium was sampled and replaced with 0.5 mL of fresh PBST at predetermined time points over two weeks. The meloxicam concentration in the sampled release medium was determined by high-performance liquid chromatography (HPLC) on an Agilent 1290 HPLC System (Agilent Technology, CA, USA) equipped with a 1290 Binary Pump, a 1290 Variable Wavelength Detector, and a 250 × 4.6 mm Luna 5 μm C18 reverse phase column (Phenomenex, CA, USA). The mobile phase consisted of 30% acetonitrile and 70% 50 mM pH 6.5 phosphate buffer (30:70, *v*/v) and flowed at 0.8 mL/min and room temperature over 15 min. Meloxicam was detected at 355 nm with a retention time of 10 min. A subset of the matrices retrieved from the 14-d *in vitro* drug release was analyzed by SEM/EDX (whole cylinder and cross-section of a cylinder exposed by a razor blade cut) and HR-μCT (whole cylinder), as described in Section 2.5. Another subset of the retrieved matrices was dissolved in tetrahydrofuran (THF) and extracted with two volumes of Tris buffer (10 mM, pH 8) to quantify the unreleased meloxicam.

2.4. Standard X-ray MicroCT

The M30/PCL matrices with or without $Mg(OH)_2$ were analyzed by a SkySkan 1272 MicroCT scanner (Bruker, Manning Park, MA). Each sample was cut into a 20 mm (length) × 0.5 mm (diameter) cylinder by a stainless-steel razor blade and mounted on a Styrofoam holder. The X-ray tube voltage and current were set at 50 kV and 120 μA with a 0.5-mm aluminum beam filter to obtain CT images with an averaged frame of 4 and random movement of 60. The stage was rotated over 180° with a rotation step of 0.12°, and the spatial resolution was set to 0.6 μm/pixel. A series of X-ray projection images were digitally computed to reconstruct 3D images. Horizontal (X-Y) and longitudinal (X-Z) cross-sections were obtained from the reconstructed images and used to compare the internal structures of the matrices.

2.5. High-resolution X-ray MicroCT (HR-μCT)

The microstructural properties of M30/PCL and M65/PCL matrices post-14-d *in vitro* drug release (Section 2.3) were visualized by HR-μCT

Table 1
Composition of hot-melt extruded mixtures of meloxicam, PCL, and salt.

HME matrices	Salt	Nominal loading (wt%)			Die orifice diameter (mm)	Measured meloxicam loading (wt%)[4]
		Meloxicam[1]	Salt[2]	PCL[3]		
M65/PCL	–	65	0	35	2.0	65.4 ± 1.2
M65/PCL	–	65	0	35	0.5	62.5 ± 4.7
M30/PCL	–	30	0	70	2.0	29.9 ± 0.2
M30/PCL	–	30	0	70	0.5	28.6 ± 0.5
M30/PCL(Mg20)	$Mg(OH)_2$	30	20	50	0.5	29.3 ± 0.2
M30/PCL(Mg35)	$Mg(OH)_2$	30	35	35	0.5	30.6 ± 1.8
M30/PCL(Mg40)	$Mg(OH)_2$	30	40	30	0.5	N.A.
M30/PCL(Mg50)	$Mg(OH)_2$	30	50	20	0.5	29.1 ± 0.1
M30/PCL(Na35)	$NaHCO_3$	30	35	35	0.5	N.A.
M30/PCL(MgPO35)	$Mg_3(PO_4)_2{\cdot}xH_2O$	30	35	35	0.5	N.A.
M30/PCL(Zn35)	ZnO	30	35	35	0.5	N.A.

N.A.: Not available.
[1] Drug loading (wt%) = Weight percentage of meloxicam in meloxicam, PCL, and salt matrix.
[2] Polymer loading (wt%) = Weight percentage of PCL in meloxicam, PCL, and salt matrix.
[3] Salt loading (wt%) = Weight percentage of salt in the total meloxicam, PCL, and salt matrix.
[4] $n = 5$ replicates of a representative batch.

imaging performed on a Zeiss Xradia 520 Versa. For the M30/PCL matrix, the X-ray tube voltage and current were set to 50 kV and 80 μA, respectively. An exposure time of 5 s was used, and 1601 projections were collected. The sample was scanned for 5 h, and the spatial resolution was set to 1.15 μm/pixel. For the M65/PCL matrix, the X-ray tube voltage and current were set to 70 kV and 85 μA, respectively. An exposure time of 4 s was used, and 1601 projections were collected. The sample was scanned for 4 h, and the spatial resolution was set to 0.76 μm/pixel.

2.6. Artificial intelligence (AI) image analysis

The μCT images were analyzed by a user-guided AI image analysis using the DigiM I2S platform. Iterative traces were performed to classify each material phase based on its grayscale contrast and morphology in order to train the machine learning algorithm. After performing the training on one to several slices from the imaging stack, the training was applied to the entire imaging stack from the HR-μCT or standard μCT scan. The classification of each phase produced a digitally transformed matrix, where drug particles, porosity, and polymer could be visualized and quantified. The size distributions, spatial uniformity, and thickness of drug-released layers were quantified directly from the 3D reconstructions of matrices. The 3D visualizations of the matrices were generated using 3D Slicer [24,25].

2.7. Imaged-based simulation of drug release kinetics

An image-based simulation was performed using the HR-μCT datasets from M30/PCL and M65/PCL matrices after the 14-d *in vitro* drug release. The unreleased drug particles and pores formed by the drug release were classified by image segmentation, as described in Section 2.6. For simulation, both the pore network (formed by the dissolution of drug particles) and the unreleased drug particles were considered drug domains, creating a time-zero sample from the reconstruction of a sample post-14-d drug release. This step assumes that the PCL matrix is sufficiently stable, and the microstructure of pores formed by drug particles would not significantly alter; thus, the corresponding pore network would be equivalent to the drug particle network. The first part of the simulation computed the amount of drug released for a series of dimensional voxel steps across the imaging data. Subsequently, the effective diffusivity changing with time was computed for each voxel step to determine how the drug particles would diffuse through an evolving porous network formed by drug particles. Finally, the information about the sample geometry, drug solubility, drug concentration (determined from known weight loading), and drug diffusion coefficients were used to convert numerical time to physical time according to the following equation, which employs the Higuchi model in a modified form:

$$t = \frac{R^2}{4\left(\frac{C_s}{C_0}\right)D_e(i)}\left[\frac{V(i)}{V_\infty} + \left(1 - \frac{V(i)}{V_\infty}\right)ln\left(1 - \frac{V(i)}{V_\infty}\right)\right] \quad (1)$$

where R is the radius of implant (assuming a cylindrical geometry); C_s the saturation solubility of a drug in the dissolution medium, C_0 the drug concentration in implant according to the drug loading content; $D_e(i)$ a multiplicate of the drug bulk diffusion coefficient and the time-changing diffusion coefficient calculated from each voxel step (i) of the simulation; $V(i)$ the volume of drug released at each voxel step (i); and V_∞ the total volume of drug in the implant.

The final output from the simulation was a drug release profile with cumulative release percentage *vs.* time. The outline of this simulation process and the associated HR-μCT and AI analysis are described in Fig. 4a. Further information about the simulation methodology can be found in the corresponding patent [26].

2.8. Scanning electron microscopy with energy dispersive X-ray analysis (SEM/EDX)

The surfaces of meloxicam-PCL matrices with or without $Mg(OH)_2$ were examined by SEM combined with EDX to visualize the drug distribution in the matrices. The meloxicam/PCL matrix with a diameter of 2 or 0.5 mm was cut into ~0.1-mm-thick discs or ~10-mm-long cylinders (Supporting Fig. 1) and mounted on an aluminum stub and sputter-coated with a thin platinum layer (Turbo-Pumped Sputter, Cressington Scientific Instruments, Watford, UK) at 40 mA for 60 s. The surfaces of the matrices were visualized with the FEI NOVA nanoSEM Field Emission SEM (FEI Company, OR, USA) at an acceleration voltage of 7 kV, a working distance of 10 mm, and a spot size of 4.5. EDX was performed with an Oxford INCA Xstream-2 silicon drift detector to determine elemental distribution in the matrices, with a magnification of 20,000 on an Xmax80 window. The data was analyzed by AZtecOne software (Oxford Instrument, Abingdon, UK).

2.9. Differential scanning calorimeter (DSC) analysis

The solid-state of raw materials and cryo-milled M30/PCL matrices with or without salts were characterized by a Q2000 DSC equipped with a refrigerated cooling accessory (TA Instruments, New Castle, DE) and purged with nitrogen at 50 mL/min. The cryo-milled samples (~3 mg) were loaded in standard aluminum pans. Meloxicam and salts were heated at 10 °C/min until the melting point was detected. The extruded

matrices and physical mixtures of the components were heated individually from 0 °C to 260 °C at 10 °C/min, then cooled to 0 °C at 10 °C/min, followed by a second heating ramp to 260 °C at 10 °C/min.

2.10. X-ray powder diffraction (XRPD) analysis

X-Ray Powder Diffraction (XRPD) analysis of PCL, meloxicam, salts, and M30/PCL matrices with or without salts was performed on a Rigaku SmartLab diffractometer (Rigaku Americas, The Woodlands, Texas). A Cu-Kα radiation source and a d/tex ultra-detector were used to collect XRPD spectra in a Bragg-Brentano mode. Prior to the measurement, approximately 5 g of the sample was milled at 5 Hz for a total of 6 min in a 6750 Freezer/Mill (SPEX, Metuchen, NJ) filled with liquid nitrogen and then placed on a glass sample holder for characterization. XRPD patterns of cryo-milled matrices and each component were obtained with a 2θ ranging from 5 to 40° and a scan rate of 10°/min using a glass sample holder.

3. Results

3.1. Preparation and characterization of M30/PCL and M65/PCL

M30/PCL and M65/PCL were extruded in two diameters, 2 mm and 0.5 mm, at 120 °C. Meloxicam has a melting temperature of 256.9 ± 0.7 °C and was previously observed to have no miscibility with PCL up to 200 °C [19]. At 120 °C, PCL with a melting temperature of 55–65 °C flowed through the extruder as liquid, whereas meloxicam flowed with the PCL as unmelted particles, as confirmed by our previous study [19]. Standard μCT analysis was performed to examine the drug distribution in the cylindrical matrices with two different diameters: 2 mm and 0.5 mm (Fig. 1). Meloxicam and PCL were identified by their density difference; PCL with a density of 1.19 g/cm^3 (as provided by the vendor) was indicated in blue, whereas meloxicam with a density of 1.69 g/cm^3 [27] was indicated in yellow. The cross-sectional images in the X-Y and X-Z axes showed that all four matrices had solid structures with few pores, where meloxicam was dispersed as clusters throughout the PCL matrix, consistent with our previous report [19].

3.2. In vitro drug release from M30/PCL and M65/PCL

The M/PCL matrices (2 mm × 0.7 mm, or 0.5 mm × 10 mm, Supporting Fig. 1) were tested for the *in vitro* drug release kinetics in PBST. The fraction of the released drug increased with the meloxicam loading

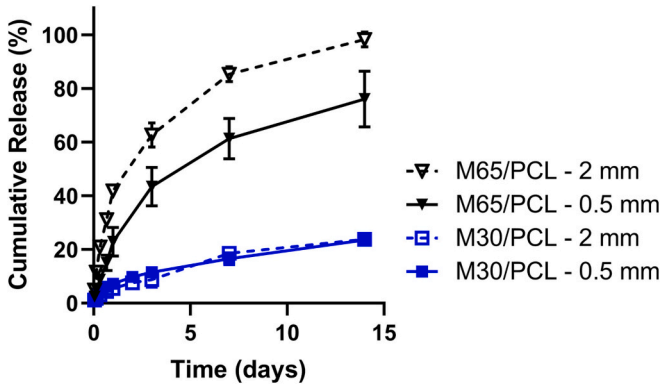

Fig. 2. *In vitro* kinetics of meloxicam release from PCL matrices with 30 wt% and 65 wt% (M30/PCL and M65/PCL) in two diameters (2 and 0.5 mm). Mean ± standard deviation (SD), n = 4–6 (2 replicates of 2–3 independently and identically produced batches). One sample was used for imaging (Fig. 1 and Fig. 3), and the other three were used for mass balance. Supporting Fig. 2 presents the data in an alternative unit on the y-axis: meloxicam (μg)/matrix (mg).

content (Fig. 2, Supporting Fig. 2), consistent with the increased channel network formation during drug release, as shown in our previous report [19]. The 2-mm and 0.5-mm matrices, with 30 wt% drug loading (M30/PCL), showed sustained drug release over 14 d up to 23.8 ± 6.7% and 23.5 ± 0.9% of the total loaded meloxicam, respectively (Fig. 2). In case of 65 wt% drug loading (M65/PCL), the 2-mm matrix and the 0.5-mm matrix released 98.2 ± 2.8% and 74.1 ± 12.7% of the total loaded drug, respectively, over 14 d (Fig. 2).

The release kinetics data were fitted to Higuchi [28], Korsmeyer-Peppas [29], and Weibull [30] release kinetic models [31]:

$$\text{Higuchi model}: \quad \frac{M_t}{M_\infty} = K_h t^{1/2} \tag{2}$$

$$\text{Korsmeyer} - \text{Peppas model}: \quad \frac{M_t}{M_\infty} = K_{kp} t^n \tag{3}$$

$$\text{Weibull model}: \quad \frac{M_t}{M_\infty} = 1 - exp\left[\frac{-(t - T_i)^b}{a}\right] \tag{4}$$

where M_t is the amount of drug released in time (t); M_t/M_∞ is the fraction of drug released; n is the release exponent that characterizes the

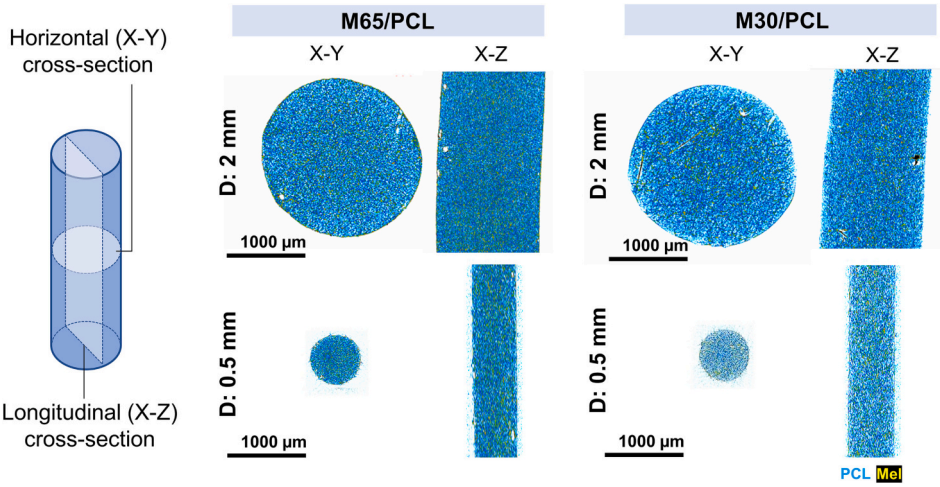

Fig. 1. Standard μCT images of cross-sections of (a) M65/PCL and (b) M30/PCL matrices in two diameters (2 and 0.5 mm). These are fresh matrices prior to *in vitro* release studies. White - pores; blue - PCL; yellow - meloxicam. (For interpretation of the references to colour in this figure legend, the reader is referred to the web version of this article.)

Table 2
Summary of drug release parameters derived from different models for release kinetics presented in Fig. 2.

M/PCL matrices		Higuchi	Korsmeyer-Peppas	Weibull
M65/PCL - 2 mm	Parameters	K_h: 30.0	K_{kp}: 34.7 n: 0.43	a: 21.7 b: 0.55
	R^2	0.945	0.975	0.688
	MAE*	6.06%	4.26%	9.43%
M65/PCL - 0.5 mm	Parameters	K_h: 20.9	K_{kp}: 21.4 n: 0.49	a: 18.7 b: 0.66
	R^2	0.981	0.982	0.787
	MAE	2.88%	2.89%	5.72%
M30/PCL - 2 mm	Parameters	K_h: 6.3	K_{kp}: 5.6 n: 0.56	a: 38.3 b: 0.52
	R^2	0.981	0.987	0.975
	MAE	0.78%	0.55%	0.75%
M30/PCL - 0.5 mm	Parameters	K_h: 6.4	K_{kp}: 7.1 n: 0.45	a: 46.1 b: 0.43
	R^2	0.992	0.998	0.993
	MAE	0.54%	0.28%	0.37%

* MAE: Mean absolute error.

mechanism of drug release; K_h and K_{kp} are release constants for Higuchi and Korsmeyer-Peppas equations, respectively; T_i represents the time lag before the onset of the release process; a defines the time scale of the process; b describes the shape of the release curve progression.

As summarized in Table 2, all four curves followed Higuchi and Korsmeyer-Peppas models with n close to 0.5, indicating that meloxicam release from the PCL matrices is mainly driven by Fickian diffusion.

It is noteworthy that the 0.5-mm M65/PCL matrix showed a slower drug release than the 2-mm M65/PCL matrix. This difference is largely driven by the extent of initial drug release. The higher initial drug release from the 2-mm matrix may have been facilitated by the cross-sectional surface area resulting from cutting (59% of the total surface area for the 2-mm matrix *vs.* 2.4% for the 0.5-mm matrix, Supporting Fig. 1), which exposes a greater proportion of encapsulated drug clusters directly to the release medium. Owing to the relatively small cross-sectional surface area, the 0.5-mm matrix would rely more on fluid infiltration into the matrix through the extruded surface and the evolution of fluid channels for drug release than the dissolution of meloxicam clusters exposed to the medium. In contrast, the M30/PCL was relatively less affected by the difference in geometry. With fewer drug clusters on the surface, either extruded side or artificially-generated cross-section, both M30/PCL matrices showed limited initial drug release irrespective of the geometry. Since the thin cylindrical matrix is more relevant to the dimensions of implants or vascular grafts, the subsequent studies were focused on the 0.5-mm matrices.

3.3. Image-based analysis of drug release kinetics from M30/PCL and M65/PCL

HR-μCT was used to image the M30/PCL and M65/PCL matrices (with a 0.5 mm diameter) completing a 14-d drug release in PBST (Fig. 3, Supporting Movies 1–2). The matrices post-14-d drug release contained an outer layer with pores (Fig. 3), indicative of vacancies initially occupied by meloxicam clusters. The matrices also contained an inner core of the meloxicam clusters indicated in lighter gray. AI image analysis was performed on the HR-μCT micrographs to classify the drug particle network, PCL, and porosity domains in 3D. The 3D microstructure network generated from the AI analysis was used to simulate the drug release kinetics (Fig. 4). According to our previous report [19], it was assumed that the drug was released as the drug clusters dissolved in the infiltrated fluid and diffused out of the PCL matrix, which is practically nondegradable in 14 d (PCL average degradation half-life: 12 months [32]). With no significant polymer degradation expected during the drug release period, the pores on the outer layer were digitally considered drug particles set to be released at time 0, and the pore network was assumed to be equivalent to the drug particle network. The 3D network of outer layer pores (*i.e.*, the spaces considered meloxicam clusters in image analysis) and unreleased meloxicam clusters, in combination, were utilized to simulate drug release kinetics and a release profile. The patented simulation suite includes a percolation simulation to determine the drug release amount at each voxel step, followed by a time-changing effective diffusivity simulation reflective of the evolving tortuous network formed by vacated drug particles.

The initial simulation of M65/PCL was consistent with the experimentally determined *in vitro* release trend (Fig. 2, Fig. 4b) with an initial burst release and a slowdown after 5 d, matching the experimental profiles across all time points. The same analysis was performed for the M30/PCL matrix with a hypothetical C_0 (*i.e.*, initial drug concentration predetermined by design, 30 wt% converted to 392 mg/mL) and the observed C_0 (only accounting for resolved drug particles, pores, and their connectivity based on the image, 176 mg/mL). In the initial simulation with the hypothetical C_0 (Fig. 4c), the simulated drug release was less than that of the M65 matrix, as seen in the *in vitro* drug release profiles (Fig. 2). This indicates that the simulation correctly captured the lower drug release due to lower drug loading and a poorer diffusion network. It also simulated the plateauing after 5 d. However, the total predicted drug release was higher than the experimentally determined release from the M30/PCL matrix. When an adjustment was made with the observed C_0, this release discrepancy increased even further (Fig. 4c). This suggests that additional factors besides diffusion may have affected the drug release from M30/PCL matrix. One potential consideration is the low connectivity of pore networks with a smaller drug content, which limits fluid infiltration into the matrix, especially at early time points. The constraint in the available fluid might have restricted drug dissolution, making the maximum concentration of dissolved drug below its saturation solubility (C_s). To explore the dissolution limit in a digital space, the entry for C_s value was adjusted from 0.099 mg/mL to 0.03 mg/mL. This adjustment improved the agreement of the image-based simulation with the *in vitro* results (Fig. 4c).

3.4. Drug release controlled by porogen encapsulation

The image-based simulation of drug release supports that the fluid infiltration and channel generation by pore networking are limited in the matrix with a lower drug loading, where the drug clusters tend to be more isolated in the polymer matrix. This is consistent with the percolation theory that describes limited drug dissolution at a drug level under the percolation threshold [33,34]. With this configuration, it is difficult to control the drug loading and release kinetics independently, especially for a practically non-degrading system where secondary release mechanisms such as polymer erosion are unavailable within the time frame of interest (*i.e.*, 14 d).

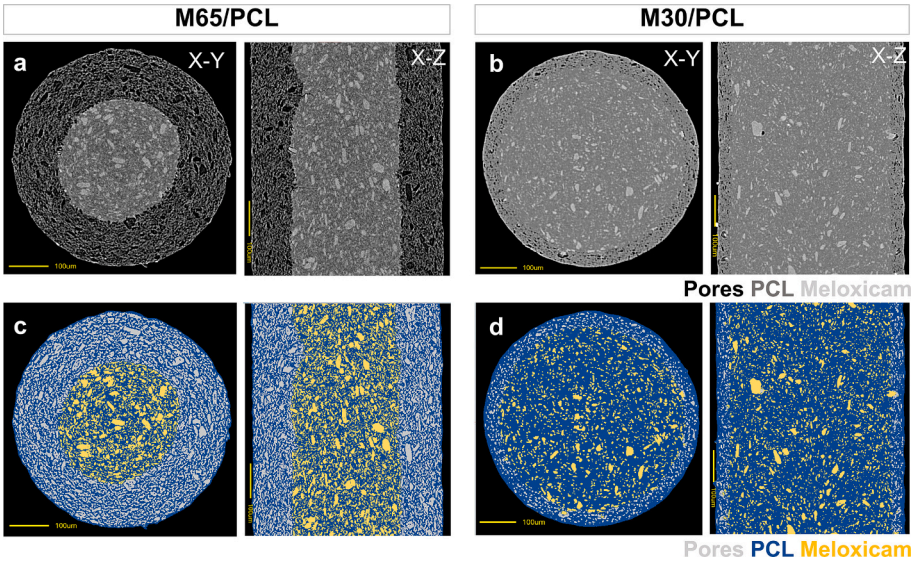

Fig. 3. (a, b) HR-μCT cross-sectional images of hot-melt extruded matrices, with 30 wt% and 65 wt% meloxicam (M30/PCL and M65/PCL, diameter: 0.5 mm), after drug release by 14 d, in original grayscale. (c, d) AI-segmented images to classify porosity and particle networks. After classification, these networks from the 3D volume are used as the direct structural input for the image-based simulation. Scale bars: 100 μm.

This limitation was overcome by investigating the inclusion of a salt porogen as an alternative way of increasing the drug-pore network connectivity and facilitating the generation of fluid channels (Table 1). $Mg(OH)_2$, $NaHCO_3$, $Mg_3(PO_4)_2{\cdot}xH_2O$, and ZnO were evaluated as candidate porogens. These salts differed in water solubility and basicity (Supporting Table 1) and were thus expected to show differential dissolution in aqueous fluid infiltrating the polymer matrix and effects on the microenvironmental pH. All salts increased the overall drug release when included at 35 wt% of the total mass, but the extent of drug release differed according to the type of salt (Fig. 5). While M30/PCL (no salt) released 18.9% of the total meloxicam in 14 d, M30/PCL(Mg35) and M30/PCL(Zn35) released 55.4% and 80.3% of the total loaded meloxicam, respectively, over 14 d. $NaHCO_3$ and $Mg_3(PO_4)_2{\cdot}xH_2O$ induced higher initial burst release of 84.1% and 60.8% in the first 24 h, and then to 94.1% and 98.5% by 3 d, respectively (Fig. 5).

The increased drug release may not be explained by the dissolution of salts in the buffer infiltrating the matrix. Both $NaHCO_3$ and $Mg_3(PO_4)_2{\cdot}xH_2O$ induced fast drug release, but the latter is not as water-soluble as the former (Supporting Table 1). Solid-state analyses were used to examine whether the salts induced differential effects on the drug crystallinity in the matrices. XRPD profiles (Supporting Fig. 3, Supporting Table 2) show that the matrices retained the diffraction patterns of meloxicam, PCL, and the included salts, providing no strong evidence to link the increased drug release rate with possible changes in the solid state of any formulation components.

To make inferences from thermal behaviors, differential scanning calorimetry (DSC) was performed for M30/PCL(Na35), M30/PCL (MgPO35), M30/PCL(Zn35), and M30/PCL(Mg35). The first heating scan showed onset melting points of 49.95 ± 0.16 °C, 50.50 ± 0.35 °C, 52.01 ± 0.17 °C, and 52.24 ± 0.14 °C, respectively, which are attributable to the melting of PCL's crystalline domains. These melting points were comparable to or slightly lower than that of M30/PCL (53.98 ± 0.04 °C) (Fig. 6, Supporting Table 3). The melting enthalpy was reduced with the inclusion of salts, *i.e.*, the reduction of polymer content (Fig. 6b). The DSC thermograms also showed broad melting endotherms of M30/PCL(Mg PO35) and M30/PCL(Na35) starting at 117 °C and 140 °C, respectively. The melting endotherms were also seen in $Mg_3(PO_4)_2{\cdot}xH_2O$ and $NaHCO_3$ (Supporting Fig. 4) as well as their physical mixtures with PCL (Fig. 6a). These endothermic transitions may be explained by the dehydration of $Mg_3(PO_4)_2{\cdot}xH_2O$ [35] and partial decomposition of $NaHCO_3$ [36], respectively. These thermal events may have led to changes in the microstructures responsible for increased water infiltration, resulting in the fast drug release from the M30/PCL (Na35) and M30/PCL(MgPO35) matrices.

Thus, the remaining viable candidates are $Mg(OH)_2$ and ZnO. $Mg(OH)_2$ was selected between the two, since micro- to nanosized ZnO is linked to severe pulmonary toxicity upon inhalation and may cause an occupational hazard during the matrix production [37].

3.5. *Effect of $Mg(OH)_2$ on meloxicam release from PCL matrices*

The $Mg(OH)_2$ content was varied from 20 wt% to 50 wt% of the total mass of the matrix. Meloxicam release from M30/PCL HME matrices (with a fixed dimension but different masses due to the density difference of components) increased with the $Mg(OH)_2$ content (Fig. 7). The $Mg(OH)_2$ containing matrices conformed to the Higuchi and Korsmeyer-Peppas models (Supporting Table 4), indicating that they also release meloxicam by Fickian diffusion. The percentages of drug release in the first 24 h for M30/PCL (Mg20), M30/PCL(Mg35), M30/PCL(Mg45), and M30/PCL(Mg50) were 21%, 29.4%, 32.6%, and 36.7%, respectively, and continuously increased in the next 13 d to 38.7%, 53.6%, 79.9%, and 96.1% of the total loaded drug. 2.1% of meloxicam was found to remain in M30/PCL(Mg50), confirming near complete drug release from the matrix. The result indicates that $Mg(OH)_2$ accelerated meloxicam release from the M30/PCL matrices over 14 d in a content-dependent manner.

3.6. *Role of $Mg(OH)_2$ in facilitating meloxicam release from M30/PCL*

The distribution of $Mg(OH)_2$ and meloxicam in M30/PCL(Mg20), M30/PCL(Mg35), and M30/PCL(Mg50) matrices was examined by standard μCT (Fig. 8, Supporting Fig. 5, Supporting movies 4–6). PCL (density: 1.19 g/cm^3, blue), meloxicam (density: 1.69 g/cm^3, yellow), and $Mg(OH)_2$ (density: 2.34 g/cm^3 [38], brown) were identified according to the density of each component (Fig. 8, Supporting movies 1–3). The cross-sectional images of fresh M30/PCL(Mg) matrices were akin to that of fresh M30/PCL matrix, mostly solid with meloxicam/salt clusters and some voids (likely to be combinations of pre-existing pores and imaging noise of standard μCT). The 3D reconstructed μCT images showed that the meloxicam/salt clusters were distributed throughout the matrices. $Mg(OH)_2$ and meloxicam clusters were visibly distinct but formed an interconnected network. The image analysis estimated the

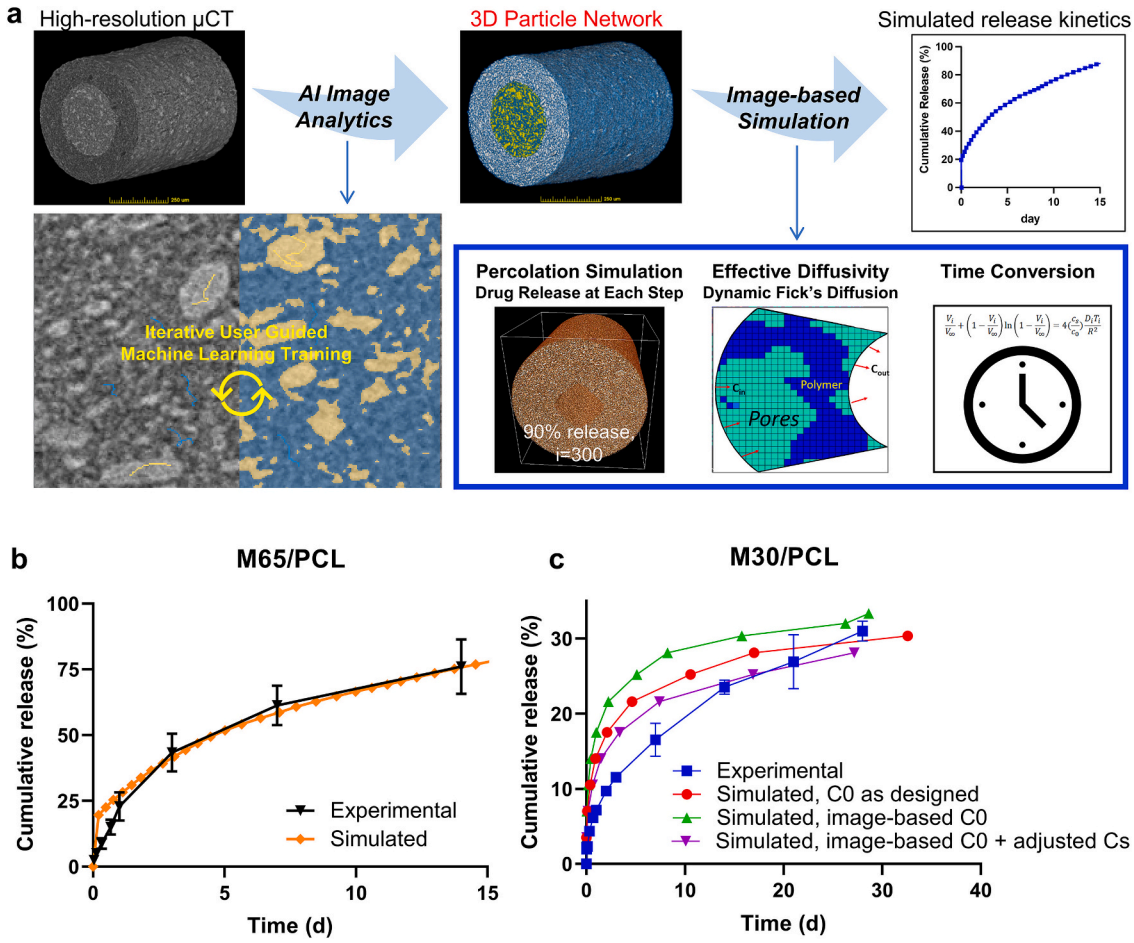

Fig. 4. (a) Workflow for AI analytics of HR-μCT images and image-based simulation of drug release from M65/PCL. The AI analysis training is performed on a small set of images and then applied to the entire image stack, creating a reconstruction of the 3D matrix with classified material domains. The image-based simulation consists of a percolation simulation, effective diffusivity calculation, and Higuchi model-based time conversion. (b) Experimentally obtained *in vitro* drug release profile (black, from Fig. 2) and simulated release profile (orange) of M65/PCL. (c) Experimentally obtained *in vitro* drug release profile (blue, from Fig. 2) and simulated release profiles of M30/PCL. Red: simulated with a C_0 as designed (hypothetical C_0); green: simulated with image-based C_0 (estimated from image analysis); purple: simulated with image-based C_0 and C_S adjusted to reflect limited dissolution in the polymer matrix. (For interpretation of the references to colour in this figure legend, the reader is referred to the web version of this article.)

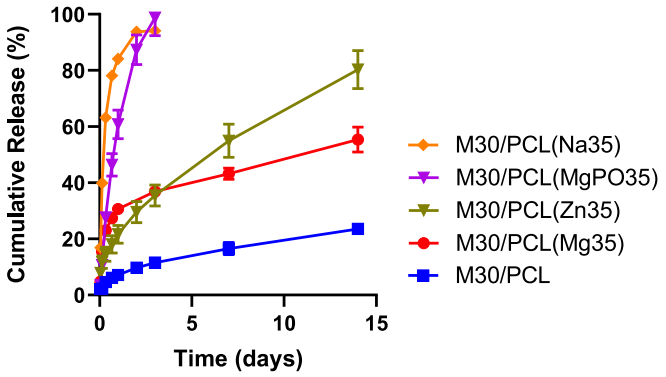

Fig. 5. *In vitro* release of meloxicam from M30/PCL (diameter: 0.5 mm) including different salts (35 wt%, Table 1). Mean ± SD; M30/PCL and M30/PCL(Mg35): $n = 4$ (2 replicates of 2 independently and identically produced batches); M30/PCL(Na35, MgPO35, or Zn35): $n = 2$ replicates of a representative batch.

weight fractions of meloxicam/salt clusters increased with the increasing $Mg(OH)_2$ contents, matching the nominal weight fractions.

In order to elucidate how $Mg(OH)_2$ facilitated drug release, the M30/PCL(Mg) matrices were imaged by SEM before and after 14-d drug release at different locations in the cross-sections (center and four side positions designated as P1-P4) followed by EDX mapping (Fig. 9, Supporting Fig. 6). Meloxicam and $Mg(OH)_2$ in the M30/PCL(Mg) were identified by sulfur (S) and magnesium (Mg), respectively, and their weight fractions relative to oxygen (O, contained in all three components: salt, meloxicam, and polymer) were quantified. In fresh M30/PCL (Mg) matrices, all five locations showed comparable S/O ratios (Fig. 9a), representing meloxicam content in the matrices, which was fixed at 30 wt%. The Mg signal and Mg/O ratio (indicating Mg contents in the matrices) increased with $Mg(OH)_2$ loading wt% (Fig. 9b) as expected. After 14-d drug release (Fig. 9c), M30/PCL(Mg20) and M30/PCL(Mg35) showed S/O ratios of 0.41 and 0.52 in the center and 0.05–0.43 and 0–0.01 in the P1–P4 positions, respectively, indicating drug depletion from the surface of matrices. M30/PCL(Mg50), which showed near complete drug release in 14 d, showed negligible S signal (0–0.02 of S/O) at all five positions (Fig. 9c). Mg/O exhibited similar patterns (Fig. 9d), with M30/PCL(Mg20) and M30/PCL(Mg35) showing lower Mg/O ratios in P1–P4 than in the center, indicating surface depletion of $Mg(OH)_2$. M30/PCL(Mg50) showed lower Mg/O ratios in all five locations compared to the other two matrices, with negligible Mg signal except for the center, indicating that $Mg(OH)_2$ followed the same fate as meloxicam. Despite signs of significant depletion of drug and salts, the SEM images 14-d drug release (Supporting Fig. 7). These observations

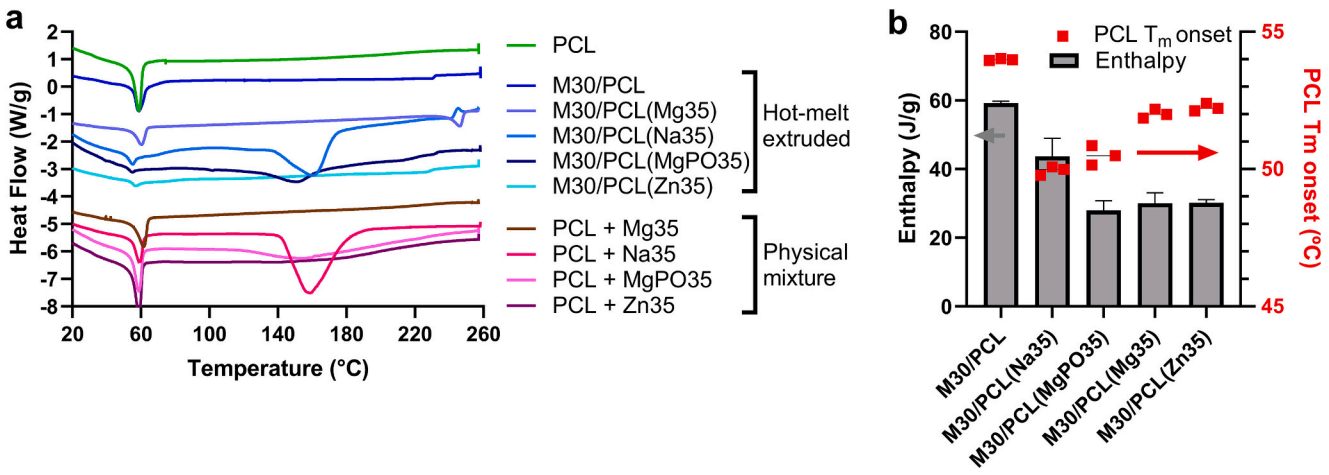

Fig. 6. (a) DSC thermograms (primary heating scan) of PCL, hot-melt extruded M30/PCL matrices with and without salts, and physical mixtures of PCL and salts (See Supporting Table 3 for composition). (b) Enthalpy and melting temperature of hot-melt extruded M30/PCL with and without salts.

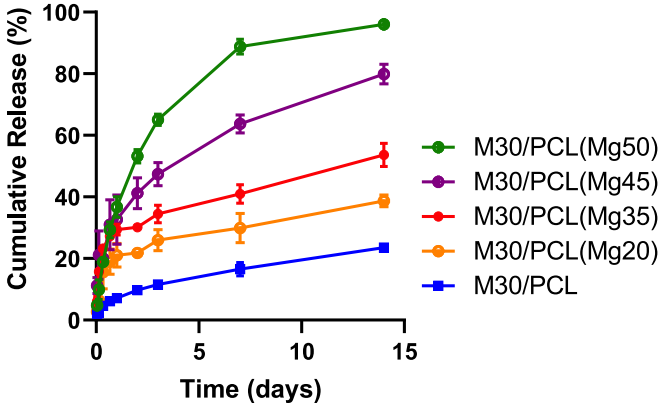

Fig. 7. *In vitro* kinetics of meloxicam release from M30/PCL matrices with 20, 35, 40, and 50 wt% of $Mg(OH)_2$. Mean ± SD, $n = 4$ (2 replicates of 2 independently and identically produced batches).

indicate that the encapsulated $Mg(OH)_2$ generated an evolving porous network, facilitating meloxicam dissolution and diffusion. The signs of remaining $Mg(OH)_2$ in the matrices suggest that $Mg(OH)_2$ dissolved over time according to the availability of medium infiltrating into the system, which is limited by the content of salt conducive to dissolution.

4. Discussion

This study reports a strategy to control drug release from polymeric matrices for local delivery of meloxicam for 14 d, a critical period during which subacute inflammations and biofilm formations are likely to occur [14]. It was previously reported that meloxicam release from PCL matrices could be controlled by the drug content [19]. However, the drug release also depends on the shape and the size of the matrix, as they determine the surface area per volume. It was observed that meloxicam release from 0.5 mm × 10 mm M65/PCL cylinder was slower than that from 2 mm × 0.7 mm M65/PCL disc (Fig. 2), even though the former had a relatively large surface area (16.1 mm^2 *vs.* 10.7 mm^2, Supporting Fig. 1). We attribute this result to the 2 mm × 0.7 mm M65/PCL matrix having a relatively large area of artificially generated cross-section, which exposed more drug to the release medium than the surface generated by extrusion. Therefore, the drug content (65 wt%) that allowed for complete drug release from the 2 mm × 0.7 mm M65/PCL matrix in 14 d was insufficient for the 0.5 mm × 10 mm M65/PCL matrix. Given the constraint in the maximum dose and the need for a polymer to form a matrix, the drug content may not be infinitely increased to afford higher drug release rates. Therefore, to deliver meloxicam by matrices with similar dimensions, such as surgical staples or injectable implants, it is necessary to find additional means to enhance meloxicam release.

The HR-μCT images of 0.5-mm M65/MCL and M30/PCL matrices completing 14-d drug release in PBST (Fig. 3) showed drug-depleted outer layers characterized by the presence of pores, indicating that the drug near the surface was released first. The drug-depleted outer layer was thicker for M65/MCL than for M30/PCL, consistent with the difference in the *in vitro* release kinetics of the two matrices (Fig. 2). The correlation between the microstructural features and the *in vitro* release kinetics allowed us to use the μCT images for simulating drug release kinetics by AI analysis. The analyses of M65/MCL and M30/PCL matrices show that the image-based simulation process helps identify critical factors contributing to drug release and complements *in vitro* release testing. The image-based simulation accurately captured the diffusion-dependent release of the M65/PCL matrix and accounted for the difference between M30/PCL and M65/PCL matrices. On the other hand, the image-based simulation of the M30/PCL matrix was different from the experimental *in vitro* results, which necessitated a digital adjustment in the C_s to reflect the limited dissolution of drug clusters in the matrix for fitting the data. This suggests that the drug release from the M30/PCL matrix depends on both dissolution and diffusion unlike the M65/PCL matrix, which has a better-connected network and hence can be described by diffusion-dependent drug release.

Given the need for enhancing drug release without relying on increasing the drug content, the matrix formulation was modified with the addition of a porogen, which can facilitate the formation of fluid channels in the matrices, thereby the diffusion of meloxicam. $Mg(OH)_2$ was the most desirable among the four salts candidates. $Mg(OH)_2$ included at 35 wt% in the M30/PCL matrix improved the cumulative drug release over 14 d from 18.9% to 55.4% of the total loaded drug (Fig. 5). $Mg(OH)_2$ has a low water solubility (6.9 μg/mL) and dissolves over time by the infiltrating fluid, unlike other porogens used in the literature, which create pre-formed pores during the production of polymeric devices [21,22]. We speculate that slowly dissolving $Mg(OH)_2$ helped not only generate fluid channels but also enhance dissolution of meloxicam in the matrix by elevating the local pH (Supporting Fig. 8). ZnO, with slightly higher solubility than $Mg(OH)_2$, showed a continuous release of 80.3% drug in 14 d (Fig. 5) but was disregarded due to the report of lung toxicity [37]. $NaHCO_3$ and $Mg_3(PO_4)_2{\cdot}xH_2O$ caused fast drug release in 3 d, which is inconsistent with our target of 14-d release. The fast drug release from M30/PCL(Na35) may be partly attributable to the high water solubility of $NaHCO_3$. Still, we cannot

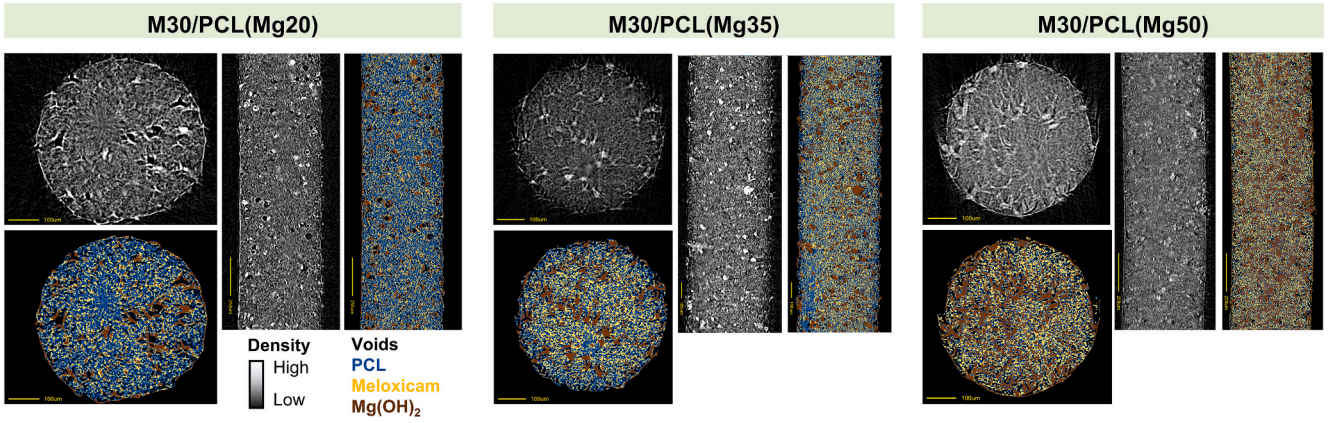

Analysis summary	M30/PCL(Mg20)	M30/PCL(Mg35)	M30/PCL(Mg50)
Voids* (vol. %)	24.2	20.3	24.3
Polymer (vol. %)	45.2	37	24.4
Meloxicam (vol. %)	19.6	25.6	26.2
$Mg(OH)_2$ (vol. %)	11	17.1	25.1
[Meloxicam+$Mg(OH)_2$]/total solid, % volume fraction	40.4	53.6	67.6
[Meloxicam+$Mg(OH)_2$]/total solid, % weight fraction	52.6	65.4	78
[Meloxicam+$Mg(OH)_2$]/total solid, nominal % weight fraction	50	65	80

Fig. 8. Image analysis of standard μCT scans of fresh M30/PCL matrices with 20, 35, and 50 wt% $Mg(OH)_2$. See Supporting Fig. 4 for additional images and dimensions. * Voids are combinations of pre-existing pores and imaging noise.

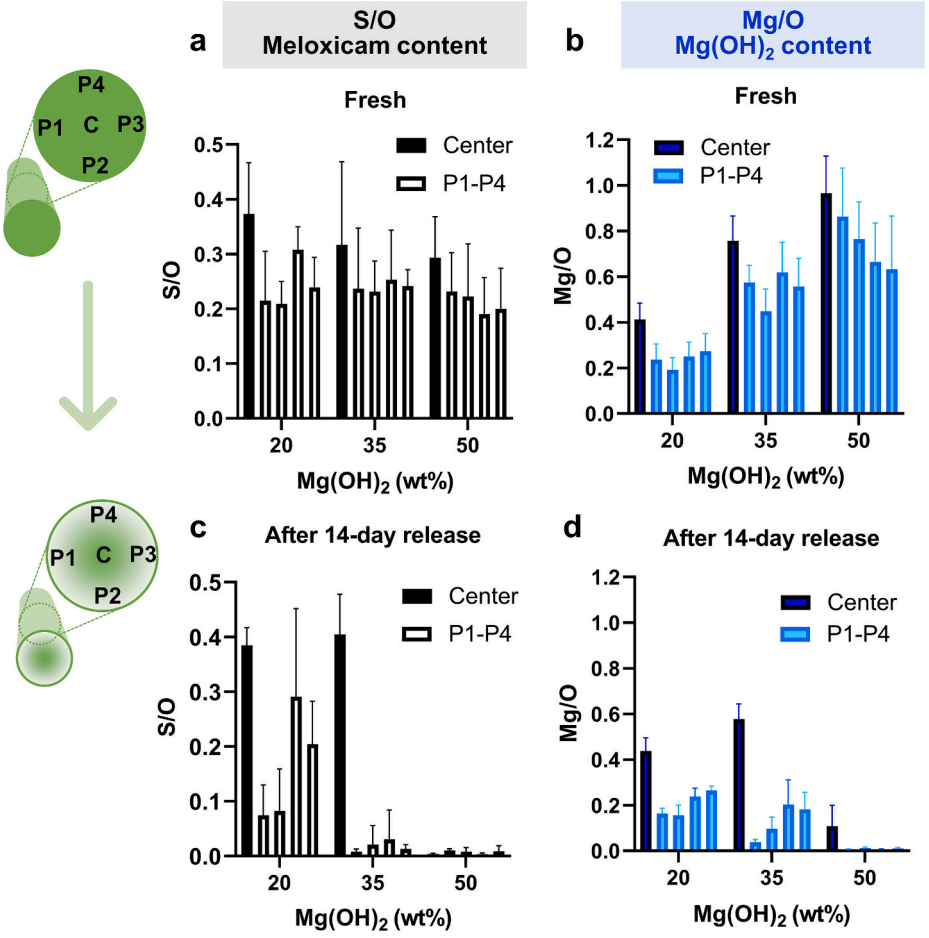

Fig. 9. SEM/EDX analysis of M30/PCL matrices with 20, 35, and 50 wt% of $Mg(OH)_2$ before (a, b) and after (c, d) *in vitro* drug release for 14 d (S: sulfur, representing meloxicam; Mg: magnesium, representing $Mg(OH)_2$). Mean ± SD, $n = 6$ (2 replicates of 3 independently and identically produced samples).

exclude the effect of thermal events during extrusion (dehydration of $Mg_3(PO_4)_2{\cdot}xH_2O$ and partial decomposition of $NaHCO_3$) on microstructures of the matrices, especially for $Mg_3(PO_4)_2{\cdot}xH_2O$, whose solubility may not explain the fast drug release from M30/PCL(MgPO35) (Fig. 6).

Meloxicam release from the M30/PCL(Mg) matrices increased in proportion to the $Mg(OH)_2$ content, resulting in almost complete drug release in 14 d from M30/PCL(Mg50) (Fig. 7). μCT and SEM/EDX of the freshly prepared matrices confirmed the increasing presence of Mg $(OH)_2$ throughout the matrices consistent with the $Mg(OH)_2$ content (Fig. 8, Fig. 9b). The SEM/EDX analysis of the M30/PCL(Mg) matrices after 14-d drug release showed fewer signals of meloxicam and $Mg(OH)_2$ in the outer layer compared to the center, irrespective of the $Mg(OH)_2$ content (Fig. 9c and Fig. 9d). This was similar to the trend observed for the drug in the M30/PCL matrix (Fig. 3). These results suggest that the drug release mechanism remained the same despite the $Mg(OH)_2$ inclusion, also supported by fitting to the mathematical models.

This study demonstrates that $Mg(OH)_2$ can accelerate the drug release from the PCL matrices, by overcoming the constraints in drug release control imposed by their geometry and dimension. As a slowly dissolving inorganic base, $Mg(OH)_2$ enhanced the drug release by providing an additional source of fluid channels in the matrices, which otherwise would have suffered from limited connectivity of the pore network. $Mg(OH)_2$ may have been additionally beneficial for the delivery of meloxicam by facilitating the dissolution of meloxicam, which is insoluble in acidic pH [19,39]. At comparable loading contents [30 wt % meloxicam *vs.* 20–35 wt% $Mg(OH)_2$], $Mg(OH)_2$ was more persistent than meloxicam in the matrix (Fig. 9c and Fig. 9d), which is likely due to the lower solubility and may have helped retain the matrix form after complete drug release (Supporting Fig. 7). The $Mg(OH)_2$ inclusion may be applicable to drug-eluting matrices with confined geometry, dimensions, and predetermined drug dose, such as surgical staples, sutures, electrospun drug-polymer composites, and injectable implants. The advantage of this strategy is that the porogen can be added to the existing combinations of drug and polymer without employing new polymers for controlling drug release kinetics.

Supplementary data to this article can be found online at https://doi.org/10.1016/j.jconrel.2023.05.049.

CRediT authorship contribution statement

Yun-Chu Chen: Conceptualization, Methodology, Investigation, Writing – original draft, Writing – review & editing, Visualization. **Sota Shishikura:** Investigation, Writing – review & editing. **Dana E. Moseson:** Investigation, Writing – review & editing. **Austin J. Ignatovich:** Investigation, Writing – review & editing. **Joshua Lomeo:** Formal analysis, Writing – review & editing, Visualization. **Aiden Zhu:** Formal analysis, Visualization. **Sarena D. Horava:** Conceptualization, Writing – review & editing. **Coralie A. Richard:** Conceptualization, Writing – review & editing. **Kinam Park:** Conceptualization, Writing – review & editing, Funding acquisition. **Yoon Yeo:** Conceptualization, Writing – original draft, Writing – review & editing, Visualization, Supervision, Project administration, Funding acquisition.

Declaration of Competing Interest

None.

Data availability

Data will be made available on request.

Acknowledgments

This study was supported by Eli Lilly and Company. The authors thank Jianchao Xu and Dr. Eric J. Munson (Purdue) for assistance in TGA analysis and Mike Shen (DigiM Solution) for assistance in model fitting and rate calculations for the *in vitro* release kinetics data. The authors also appreciate the administrative support of Drs. Thomas R. Verhoeven and James H. Parshall, and technical support of Dr. Monica Rixman Swinney. Reshma Bharadwaj provided editing support.

References

[1] Y.-C. Chen, S.F. Gad, D. Chobisa, Y. Li, Y. Yeo, Local drug delivery systems for inflammatory diseases: status quo, challenges, and opportunities, J. Control. Release 330 (2021) 438–460.
[2] B. Joseph, A. George, S. Gopi, N. Kalarikkal, S. Thomas, Polymer sutures for simultaneous wound healing and drug delivery–a review, Int. J. Pharm. 524 (2017) 454–466.
[3] J.S. Boateng, H.V. Pawar, J. Tetteh, Polyox and carrageenan based composite film dressing containing anti-microbial and anti-inflammatory drugs for effective wound healing, Int. J. Pharm. 441 (2013) 181–191.
[4] C. Pawlukianiec, M.E. Gryciuk, K.M. Mil, M. Żendzian-Piotrowska, A. Zalewska, M. Maciejczyk, A new insight into meloxicam: assessment of antioxidant and anti-glycating activity in in vitro studies, Pharmaceuticals 13 (2020) 240.
[5] A. Nienaber, F.E. Hayford, E. Variava, N. Martinson, L. Malan, The manipulation of the lipid mediator metabolism as adjunct host-directed therapy in tuberculosis, Front. Immunol. 12 (2021), 623941.
[6] A. Bekker, C. Kloepping, S. Collingwood, Meloxicam in the management of post-operative pain: narrative review, J. Anaesthesiol. Clin. Pharmacol. 34 (2018) 450.
[7] S.A. Hussain, B.H. Marouf, Z.S. Ali, R.S. Ahmmad, Efficacy and safety of co-administration of resveratrol with meloxicam in patients with knee osteoarthritis: a pilot interventional study, Clin. Interv. Aging 13 (2018) 1621.
[8] J.-E. Pan, F.-L. Xiong, G. Chen, Z.-W. Zhang, Y.-J. Xu, Aquaporin-1 expression as an indicator in evaluating the efficacy of meloxicam in the treatment of ankylosing spondylitis: a comparative study, Biomed. Pharmacother. 95 (2017) 1549–1555.
[9] B.H. Marouf, S.A. Hussain, Z.S. Ali, R.S. Ahmmad, Resveratrol supplementation reduces pain and inflammation in knee osteoarthritis patients treated with meloxicam: a randomized placebo-controlled study, J. Med. Food 21 (2018) 1253–1259.
[10] M. Orozco-Solís, Y. García-Ávalos, C. Pichardo-Ramírez, F. Tobías-Azúa, J.-R. Zapata-Morales, O.-H. Aragon-Martínez, M.-A. Isiordia-Espinoza, Single dose of diclofenac or meloxicam for control of pain, facial swelling, and trismus in oral surgery, Med. Oral Patol. Oral Cir. Bucal. 21 (2016), e127.
[11] P. She, Y. Wang, Z. Luo, L. Chen, R. Tan, Y. Wang, Y. Wu, Meloxicam inhibits biofilm formation and enhances antimicrobial agents efficacy by *Pseudomonas aeruginosa*, MicrobiologyOpen 7 (2018), e00545.
[12] A. Bekker, C. Kloepping, S. Collingwood, Meloxicam in the management of post-operative pain: narrative review, J. Anaesthesiol. Clin. Pharmacol. 34 (2018) 450–457.
[13] R.D. Berkowitz, R.J. Mack, S.W. McCallum, Meloxicam for intravenous use: review of its clinical efficacy and safety for management of postoperative pain, Pain Management 11 (2021) 249–258.
[14] H.P. Sandoval, L.E.F. de Castro, D.T. Vroman, K.D. Solomon, A review of the use of ketorolac tromethamine 0.4% in the treatment of post-surgical inflammation following cataract and refractive surgery, Clin. Ophthalmol. 1 (2007) 367.
[15] R. Pahwa, A. Goyal, I. Jialal, Chronic Inflammation, StatPearls, 2021.
[16] N. Fernández, E.E. Díaz, R. Amils, J.L. Sanz, Analysis of microbial community during biofilm development in an anaerobic wastewater treatment reactor, Microb. Ecol. 56 (2008) 121–132.
[17] T. Bjarnsholt, K. Buhlin, Y. Dufrêne, M. Gomelsky, A. Moroni, M. Ramstedt, K. Rumbaugh, T. Schulte, L. Sun, B. Åkerlund, Biofilm Formation–What We Can Learn From Recent Developments, Wiley Online Library, 2018, pp. 332–345.
[18] H. Zhao-Fleming, A. Hand, K. Zhang, R. Polak, A. Northcut, D. Jacob, S. Dissanaike, K.P. Rumbaugh, Effect of non-steroidal anti-inflammatory drugs on post-surgical complications against the backdrop of the opioid crisis, Burns Trauma 6 (2018) 25.
[19] Y.-C. Chen, D.E. Moseson, C.A. Richard, M.R. Swinney, S.D. Horava, K.A. Oucherif, A.L. Cox, E.D. Hawkins, Y. Li, D.F. DeNeve, Development of hot-melt extruded drug/polymer matrices for sustained delivery of meloxicam, J. Control. Release 342 (2022) 189–200.
[20] F. Karaaslan, Ş. Erdem, M.U. Mermerkaya, Wound management with vacuum-assisted closure in postoperative infections after surgery for spinal stenosis, Intern. Med. Case Reports J. 8 (2015) 7.
[21] V. Santos-Rosales, I. Ardao, L. Goimil, J.L. Gomez-Amoza, C.A. García-González, Solvent-free processing of drug-loaded poly (ε-caprolactone) scaffolds with tunable macroporosity by combination of supercritical foaming and thermal porogen leaching, Polymers 13 (2021) 159.
[22] T. Waterkotte, X. He, A. Wanasathop, S.K. Li, Y.C. Park, Long-term antibody release polycaprolactone capsule and the release kinetics in natural and accelerated degradation, ACS Biomater. Sci. Eng. 8 (2022) 4428–4438.
[23] U. Pharmacopeia, USP-NF <1092> The Dissolution Procedure: Development and Validation, USP 32-NF27, in: https://www.uspnf.com/notices/general-chapter-dissolution-procedure-development-and-validation, 2009.
[24] 3D Slicer as a Platform. https://www.slicer.org/wiki/CitingSlicer.
[25] A. Fedorov, R. Beichel, J. Kalpathy-Cramer, J. Finet, J.-C. Fillion-Robin, S. Pujol, C. Bauer, D. Jennings, F. Fennessy, M. Sonka, 3D slicer as an image computing platform for the quantitative imaging network, Magn. Reson. Imaging 30 (2012) 1323–1341, https://doi.org/10.1016/j.mri.2012.05.001.

[26] S. Zhang, System and Method for Computing Drug Controlled Release Performance Using Images, United State Patents 11,081,212 B2, 2023.
[27] Meloxicam. https://www.chemicalbook.com/ProductMSDSDetailCB2191355_EN.htm.
[28] T. Higuchi, Mechanism of sustained-action medication. Theoretical analysis of rate of release of solid drugs dispersed in solid matrices, J. Pharm. Sci. 52 (1963) 1145–1149.
[29] R.W. Korsmeyer, R. Gurny, E. Doelker, P. Buri, N.A. Peppas, Mechanisms of solute release from porous hydrophilic polymers, Int. J. Pharm. 15 (1983) 25–35.
[30] F. Langenbucher, Linearization of dissolution rate curves by the Weibull distribution, J. Pharm. Pharmacol. 24 (1972) 979–981.
[31] P. Costa, J.M. Sousa Lobo, Modeling and comparison of dissolution profiles, Eur. J. Pharm. Sci. 13 (2001) 123–133.
[32] M. Bartnikowski, T.R. Dargaville, S. Ivanovski, D.W. Hutmacher, Degradation mechanisms of polycaprolactone in the context of chemistry, geometry and environment, Prog. Polym. Sci. 96 (2019) 1–20, https://doi.org/10.1016/j.progpolymsci.2019.05.004.
[33] T. Wenzel, C. Stillhart, P. Kleinebudde, A. Szepes, Influence of drug load on dissolution behavior of tablets containing a poorly water-soluble drug: estimation of the percolation threshold, Drug Dev. Ind. Pharm. 43 (2017) 1265–1275.
[34] G. Di Colo, Controlled drug release from implantable matrices based on hydrophobia polymers, Biomaterials 13 (1992) 850–856.
[35] N. Petranović, U. Mioč, D. Minić, Kinetic aspects of the thermal treatment of acid crystallohydrate, MgHPO4· 3H2O: part 2. Dehydration and accompanying effects, Thermochim. Acta 116 (1987) 137–143, https://doi.org/10.1016/0040-6031(87)88173-X.
[36] M. Hartman, K. Svoboda, M. Pohořelý, M. Šyc, Thermal decomposition of sodium hydrogen carbonate and textural features of its calcines, Ind. Eng. Chem. Res. 52 (2013) 10619–10626, https://doi.org/10.1021/ie400896c.
[37] C. Monsé, M. Raulf, B. Jettkant, V. van Kampen, B. Kendzia, L. Schürmeyer, C. E. Seifert, E.-M. Marek, G. Westphal, N. Rosenkranz, Health effects after inhalation of micro-and nano-sized zinc oxide particles in human volunteers, Arch. Toxicol. 95 (2021) 53–65, https://doi.org/10.1007/s00204-020-02923-y.
[38] R. Ropp, Group 16 (O, S, Se, Te) alkaline earth compounds, Encycl.Alkaline Earth Comp. (2013) 105–197, https://doi.org/10.1016/C2012-0-00777-6.
[39] P. Sieger, Y. Cui, S. Scheuerer, pH-dependent solubility and permeability profiles: a useful tool for prediction of oral bioavailability, Eur. J. Pharm. Sci. 105 (2017) 82–90, https://doi.org/10.1016/j.ejps.2017.04.016.